Journal of the Optical Society of America B
OPTICAL PHYSICS

Bandpass notch filter based on valley photonic crystals

GANG LI, JUNHAO YANG, CHENYANG PENG, CHUNLIN MA, AND XINYUAN QI*

School of Physics, Northwest University, 710127, Xi'an, China
**qixycn@nwu.edu.cn*

Received 3 March 2025; revised 19 May 2025; accepted 27 May 2025; posted 27 May 2025; published 16 June 2025

As one of the core components of quantum photonics, optical filtering devices play a pivotal role in the manipulation of photonic signals. Conventional filters are generally limited to single-function operations, such as bandpass or bandstop filtering, which fall short of addressing the demand for coordinated control of broadband transmission and narrowband suppression in complex optical systems. To overcome this challenge, we propose a valley photonic crystal (VPC)-based bandpass notch filter that integrates the dual functionalities of bandpass filtering and notch filtering. The core structure of this device is constructed by coupling a topological straight waveguide with a triangular resonant cavity, enabling highly efficient optical signal transmission across a broad frequency spectrum while achieving precise suppression of targeted narrowband noise. By breaking the symmetry of a hexagonal lattice, we designed an all-dielectric silicon-based VPC structure supporting topological edge states, achieving a wide TE-polarized bandgap spanning 171.97–194.06 THz and a high-Q resonant mode ($Q \approx 3.5226 \times 10^8$) at 185.77 THz via the spin-valley locking effect. Through single- and dual-cavity coupling configurations, we demonstrate flexible filtering characteristics in the frequency ranges of 178.0–178.8 THz and 185.4–186.0 THz, with a notch bandwidth as narrow as 0.01 THz. Simulation results validate the flexibility of this design principle and provide an innovative approach for realizing frequency-selective notch filters with high precision. This design can be readily integrated with quantum photonic chips, offering promising potential for applications in on-chip optical communications and integrated photonic devices.

https://doi.org/10.1364/JOSAB.561094

1. INTRODUCTION

As one of the fundamental building components of micro–nano optical devices, the photonic crystal filter [1–3] plays an indispensable role in numerous optical scientific research and application scenarios. Due to its photonic bandgap effect, it can selectively block optical signals in non-target wavelength bands without interfering with the entire passband. By introducing defects into the photonic crystal, researchers can fabricate transmission waveguides and micro-ring resonators, thus enabling the selective transmission of light at specific wavelengths [4–11]. However, when the optical signals propagating within the micro-ring resonators encounter sharp bends, an inevitable and non-negligible reflection always occurs, reducing the transmission efficiency. In addition to the issue of reflection at sharp bends, in experiments, the surface roughness of the micro-ring resonators can give rise to the backscattering of light. Moreover, the coupling between the forward and backward transmission modes may also lead to the splitting of resonant modes and the distortion of the Lorentzian-shaped spectrum [12]. With the continuous advancement of micro–nano processing technologies [13–17], avoiding some of these situations is possible. However, due to the inherent working principle of micro-ring resonators, the backscattering of light waves is inevitable. Despite the progress in fabrication techniques that can mitigate certain negative effects, the fundamental nature of the micro-ring resonator operation dictates that backscattering remains an inescapable factor that affects the device's performance.

In recent years, topological photonic crystals have garnered extensive attention due to their unique light control mechanisms, such as scattering-immune light propagation and defect modes within topological bandgaps. High-performance on-chip topological photonic crystal devices, including topological power splitters [18–22], wavelength division multiplexers and demultiplexers [23–26], topological rainbows [27–30], and topological filters [3,31–33], have been successfully realized. Many related papers have deeply discussed topological filters based on topological photonic crystals. For example, they mentioned add/drop filters with low-power tuning using silicon's thermo-optic effect [34], and band-stop filters (BSFs) with different bandwidths by changing the liquid crystal's refractive index [35]. Additionally, based on the topological protection properties, light waves can effectively resist interference from sharp angles, bends, and other complex geometric structures

during transmission, allowing for the design of compact optical topological cavities of arbitrary shapes [36–38]. This lays a solid foundation for constructing large-scale, highly robust photonic circuits on a single chip and opens up significant potential for developing integrated photonic systems.

In this work, we propose a topological photonic crystal-based bandpass notch filtering structure [39], which integrates both bandpass and notch functionalities into a single optical filter. The core of the device consists of a topological straight waveguide and a triangular resonant cavity. The topological straight waveguide and the triangular resonator are designed based on two distinct edge states, incorporating both single-cavity and dual-cavity configurations. By designing the coupling mode between the topological straight waveguide and the triangular resonator, the structure realizes the notching function for the optical signal of a specific frequency and, at the same time, presents the selective passage characteristics of the optical signal of other frequencies. By simulating the transmission process of light waves in the structure, the results fully verify that the structure can accurately filter the optical signal at a specific frequency as a bandpass-notch filter. It is worth noting that through the reasonable combination of triangular resonators with different side lengths, multiple resonant frequencies can appear in a relatively short band, and the emergence of these multiple resonant frequencies effectively improves the filtering performance of the filter, so that it can selectively filter the light waves of a specific frequency more accurately and greatly improves the frequency selectivity and resolution of the filter. These research results can provide diversified and valuable research ideas and implementations for improving the performance of topological band notch filters.

2. THEORY AND MODEL

The structure of the valley photonic crystal is composed of triangular air holes with two different side lengths, which are arranged in a honeycomb lattice, as shown in Fig. 1(a). By destroying the size of the two cell sizes, the lattice symmetry is changed from C_{6v} symmetry to C_{3v} symmetry, and the symmetry of the structure is reduced so that the degeneracy of the K point and the K′ point energy valley is opened, and the topological phase transition occurs [40]. The side lengths of the triangular air holes are adjusted from the initial $d_A = d_B = 0.6a$ to $d_A = 0.6a$ and $d_B = 0$ (or $d_B = 0.6a$ and $d_A = 0$), where the lattice constant $a = 350$ nm. After the above structural adjustments, Fig. 1(b) shows that the Dirac points are opened, generating a TE polarization bandgap ranging from 171.97 to 194.06 THz. A wide topological photonic bandgap is a prerequisite for achieving a wide operating bandwidth for the valley photonic crystal structure. In view of this, this study delves deeply into the relationship between the operating bandwidth of the VPC 1 structure and the side length d_B of the air column. The research results show that as the side length d_B of the air column gradually increases, the topological photonic bandgap exhibits a blue shift phenomenon, and simultaneously, the operating bandwidth also shows a tendency to gradually narrow, as depicted in Fig. 1(c). When left-handed circularly polarized light (LCP) and right-handed circularly polarized light (RCP) excite the VPC 1 and VPC 2 structures, respectively,

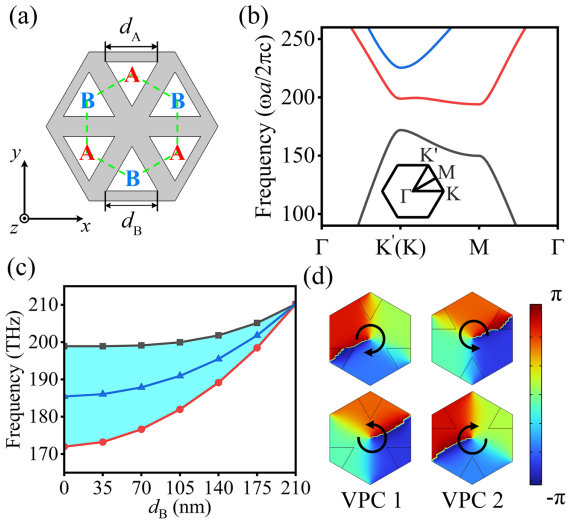

Fig. 1. Schematic and operation principle of the VPCs. (a) The green dashed hexagon in the figure represents the unit cell of the valley photonic crystal ($d_A = d_B = 0.6a$), where the lattice constant $a = 350$ nm. (b) The band structures of VPC 1 ($d_A = 0.6a$ and $d_B = 0$) and VPC 2 ($d_B = 0.6a$ and $d_A = 0$) are shown, with the TE-polarized bandgap ranging from 171.97 to 194.06 THz. (c) A diagram illustrating the relationship between the photonic bandgap and the center frequency of VPC 1 as a function of the air column side length d_B. (d) The phase distribution of the magnetic field component H_z [i.e., arg(H_z)] corresponding to the K′ valley for both VPC 1 and VPC 2 is depicted.

the phase distributions of the magnetic field H_z component at the K′ valley and K valley are shown in Fig. 1(d). Light with different polarization states demonstrates distinct phase vortex characteristics in the aforementioned valleys. This discovery provides a new perspective for a deeper understanding of the optical properties of valley photonic crystals.

Based on the $k \cdot p$ model [41,42], the effective Hamiltonian around the K/K′ valleys can be expressed as

$$H_{K/K'} = \pm\left(v_D \delta \boldsymbol{k}_x \sigma_x + v_D \delta \boldsymbol{k}_y \sigma_y\right) \pm m v_D^2 \sigma_z, \quad (1)$$

where v_D is the group velocity, $\delta k_i = k - k_{K/K'} (i = x, y, z)$ is the inverted spatial displacement from the wave vector to the valley, σ_x, σ_y, and σ_z are the Pauli matrix, and m is the effective mass [41]. The Chern number of K/K′ valley is $C_{K/K'} = \pm \mathrm{sgn}(m) = \pm\frac{1}{2}$. The topological protection characteristics of the VPCs system are defined by $C_v = C_K - C_{K'}$; i.e., $C_{v1} = 1$ for VPC 1 and $C_{v2} = -1$ for VPC 2 [43]. The two edge states are respectively locked to the K and K′ valleys, which refers to the "valley-locked" chirality.

The two types of edge states, VPC 1 and VPC 2, are edge states with different topological attributes, edge state 1 (red) and edge state 2 (blue). To compare the performance of the two types of edge states, as shown in Figs. 2(a) and 2(b), in this study, a supercell is extracted from the VPCs system to analyze the properties of the edge states. The finite element software is used to apply periodic edge conditions in the x-direction of the supercell, and the lattice length is $a = 350$ nm. In the y-direction, the length is approximately 10 μm (10 layers). By calculating the eigenmodes of the supercell with the wave vector (ranging from 0 to $\frac{\pi}{a}$), we obtain the corresponding band

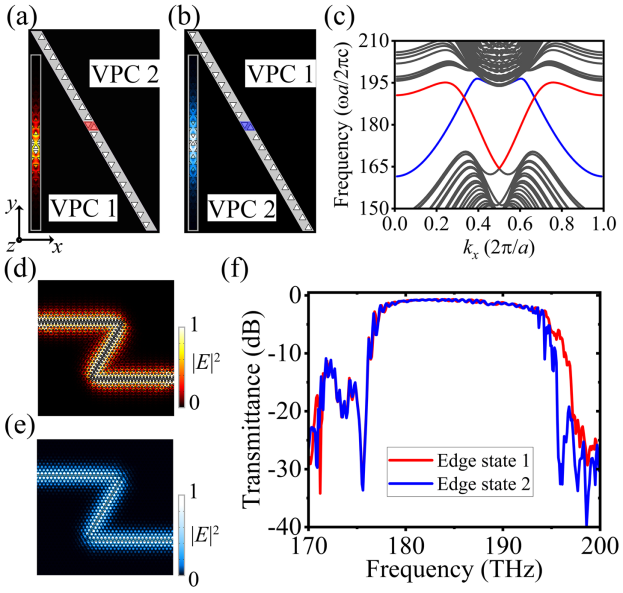

Fig. 2. Schematic and simulation results of edge states in topological photonic crystals. (a) and (b) are the basic structures of edge state 1 and edge state 2 in a period in the x-direction, with gray and white areas representing silicon and air, respectively. The inset shows the electric field amplitude patterns for edge state 1 and edge state 2. (c) Dispersion curves for the two edge states supported by edge states 1 (red) and 2 (blue). (d) and (e) Electric field amplitude patterns of Z-type transmission waveguides with different edge states at a centre frequency of 183.02 THz. (f) Transmittance curves of Z-type transmission waveguides in different edge states.

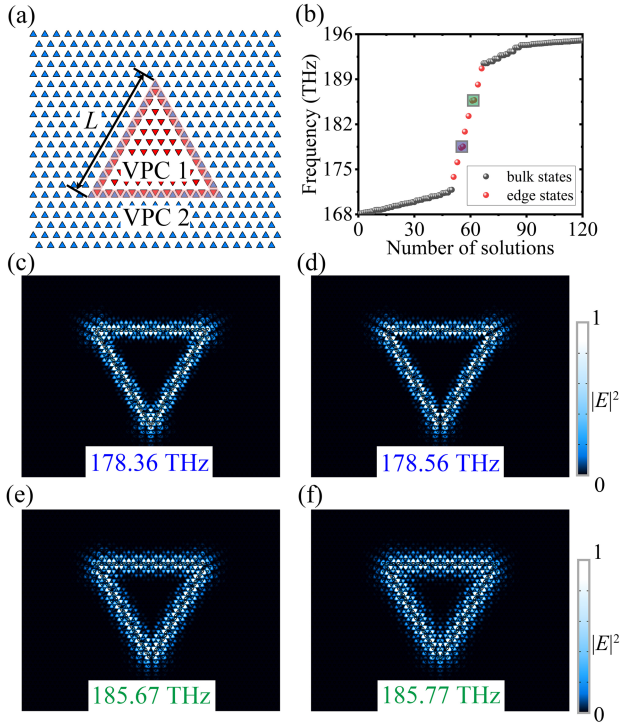

Fig. 3. Simulation of electric field distributions in a triangular resonator based on edge state 2. (a) A schematic diagram of the structure of a triangular resonator based on edge state 2. (b) The intrinsic frequencies of the structure in (a). (c)–(f) The electric field amplitude intensity distributions of the triangular resonator at frequencies 178.36, 178.56, 183.67, and 185.77 THz, respectively.

structure, as shown in Fig. 2(c). The band structure of edge state 1 (edge state 2) is marked with red (blue). To further verify the topologically robust transmission of the valley edge states, this study constructs a Z-shaped waveguide structure with edge states bent at two sharp angles of 60°, as shown in Figs. 2(d) and 2(e). Numerical simulations reveal that within the topological photonic bandgap, waveguides with two distinct edge types exhibit exceptional light-field localization characteristics. As shown in Fig. 2(f), electromagnetic energy remains tightly confined to the interface region and propagates along the heterostructure boundary without scattering losses. At the central frequency of 183.02 THz, the structure achieves a high transmission efficiency with an insertion loss (IL) of only 0.67 dB, directly demonstrating the defect immunity of valley-edge states through energy transport metrics. These results confirm the topological robustness of the valley-edge states and validate the effectiveness and reliability of the proposed waveguide design.

Unlike the transmission in traditional waveguides, the transmission of topological edge states is hardly affected by sharp corners. Therefore, we designed and constructed a triangular resonant cavity composed of VPC 2 outside the cavity and VPC 1 inside the cavity, as shown in Fig. 3(a). In this triangular resonant cavity, the side length ($L = 24a$) significantly impacts the number and position of the resonant frequencies of the cavity. The corresponding eigenfrequencies of the combined structure are displayed in Fig. 3(b), with the red and gray points representing the edge and bulk states, respectively. The electric field profiles of the eigenmode of the edge states at 178.36, 178.56, 185.67, and 185.77 THz are displayed in Figs. 3(c)–3(f), respectively.

These electric field distribution images show that these edge state patterns are topologically protected, resulting in very weak light scattering even at the sharp corners of the triangular resonator. These edge state modes all have high Q values of 6.673×10^7, 7.6809×10^7, 3.4502×10^8, and 3.5226×10^8 at the resonant frequencies of 178.36, 178.56, 185.67, and 185.77 THz, respectively. It should be noted that the Q value ($\lambda/\Delta\lambda$) is defined as the ratio of the operating wavelength (λ) to the half-height width of the formant peak ($\Delta\lambda$) [44–46], which is an important indicator of the performance of the resonator.

We further combine a triangular resonator (edge state 2) and a topological straight waveguide (edge state 1) into a bandpass notch filter system, as shown in Fig. 4(a). In this system, the effective coupling of edge state 1 and edge state 2 is realized. According to the time-domain coupling mode theory (CMT) [47,48], the relationship between the amplitude of the normalized mode a_0 in the resonator cavity and the time t is as follows:

$$\frac{da_0}{dt} = \left(j\omega_0 - \frac{1}{\tau_0} - \frac{1}{\tau_1} - \frac{1}{\tau_2}\right) a_0 + \sqrt{\frac{2}{\tau_1}} S_{+1} + \sqrt{\frac{2}{\tau_2}} S_{+2}, \tag{2}$$

where τ_0 is the amplitude decay time of the internal loss of the resonant cavity; τ_1 and τ_2 are, respectively, the amplitude decay times of the losses generated by the coupling

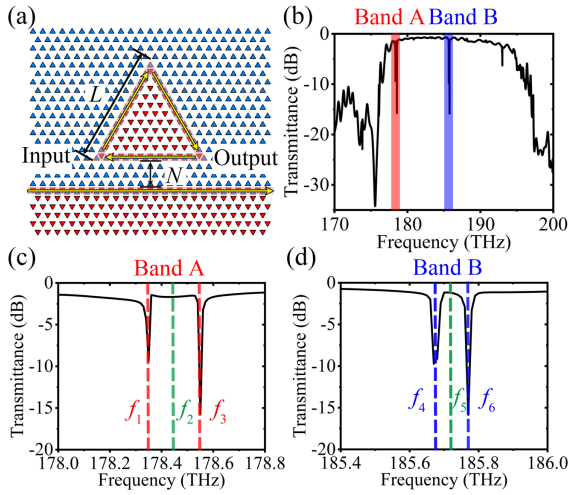

Fig. 4. Schematic and simulation results of the bandpass notch filter. (a) A schematic diagram of the structure of a bandpass notch filter composed of a triangular resonator and a topological straight waveguide. (b) The transmittance curve of the bandpass notch filter. (c) and (d) Transmittance curves of the bandpass notch filter within B and A (178.0–178.8 THz) and Band B (185.4–186.0 THz), respectively.

between the resonant cavity and the two ends of the waveguide; $S_{+i}(i = 1, 2)$ are, respectively, the input waves at the two ports of the waveguide; and ω_0 is the frequency of the localized light in the micro-cavity. According to time reversal and power conservation, it can be obtained that

$$S_{-1} = S_{+2} - \sqrt{\frac{2}{\tau_1}} a_0, \tag{3}$$

$$S_{-2} = S_{+1} - \sqrt{\frac{2}{\tau_2}} a_0, \tag{4}$$

where $S_{-i}(i = 1, 2)$ represents the reflected wave. When there is only input from one port, that is, $S_{+1} = 0$ or $S_{+2} = 0$, the coupling transmission efficiency between the straight waveguide and the micro-cavity is expressed as

$$T = \left| \frac{\mathrm{j}(\omega - \omega_0) + \frac{1}{\tau} - \sqrt{\frac{4}{\tau_1 \tau_2}}}{\mathrm{j}(\omega - \omega_0) + \frac{1}{\tau}} \right|^2, \tag{5}$$

where $\frac{1}{\tau} = \frac{1}{\tau_0} + \frac{1}{\tau_1} + \frac{1}{\tau_2}$.

As expected, the bandpass notch filter exhibits high transmittance over the operating bandwidth, as shown in Fig. 4(b). The transmittance spectrum clearly shows that the resonant frequency is mainly concentrated in two specific bands, namely Band A (178.0–178.8 THz) and Band B (185.4–186.0 THz). In order to analyze the filtering characteristics of these two bands in more detail, we plotted the correlation transmittance spectra of Band A and Band B, respectively, as shown in Figs. 4(c) and 4(d). As shown in Fig. 4, key performance parameters of the photonic crystal filter can be derived, including the suppression ratio (SR), roll-off rate (ROR), and shape factor (SF), as summarized in Table 1. It has been discovered that the coupling spacing N between the triangular resonator and the topological straight waveguide exerts a significant influence on the coupling effect of light waves. When the coupling spacing N is within a specific range, compared with the eigenfrequency of the previous triangular resonator with an edge length of $L = 24a$, the number of resonant peaks remains unchanged, yet the positions of the resonant peaks exhibit slight shifts. This phenomenon shows that at this spacing, the system is close to a critical coupling condition [49]. Consequently, the coupling spacing between the triangular resonator and the topological straight waveguide can serve as a parameter for adjusting the filtering performance of the bandpass notch filter.

Table 1. Calculated Parameters of the Bandpass Notch Filter

Parameter	Symbol	Typical Value	Unit
3 dB bandwidth	BW_3 dB	0.01–0.03	THz
Suppression ratio	SR	9.38–15.85	dB
Roll-off rate	ROR	648.18–1294.4	dB/THz
Shape factor	SF	1.34–1.67	–
Insertion loss	IL	0.67–2.68	dB

To conduct an in-depth and comprehensive exploration of the coupling effect between the topological straight waveguide and the triangular resonator, we simulated the electric field strength distributions at the resonant frequencies and the transmitted frequencies, as illustrated in Fig. 5. It can be observed that, in the electric field intensity distributions of the resonant frequencies f_1, f_3, f_4, and f_6, most of the light field is confined to the triangular resonator, which is attributed to the fact that the coupling between the topological straight waveguide and the triangular resonator reaches the proximity coupling condition at these specific resonant frequencies. In contrast, in the electric field intensity distribution of the transmitted frequencies f_2 and f_5, the light wave will return to the topological straight waveguide again through coupling into the triangular resonator after being coupled to the topological straight waveguide and finally output to the outlet port on the right. This light field distribution characteristic shows that the coupling mechanism of the system changes at the transmission frequencies f_2 and f_5, and the light can be smoothly transmitted and exchanged between the topological straight waveguide and the triangular resonator, and the effective transmission of the optical signal is realized. Based on the above analysis, the bandpass notch filter structure realizes the filtering effect in the working frequency range, which shows that the structure can accurately filter out the optical signal transmission of a particular channel without interference from other channels. This feature stems from the system's selective coupling and transmission mechanism for different frequency optical signals, which changes the coupling efficiency and transmission path of the light between the waveguide and the resonator by adjusting the frequency of the light.

In order to improve the performance of the filter, we consider the method of combining resonant cavities with different side lengths. Due to the unique geometry of resonators with different side lengths, the corresponding resonant frequency positions are also different. Based on this characteristic, the structure formed by combining resonators with different side lengths is expected to allow multiple resonant frequencies to occur in a

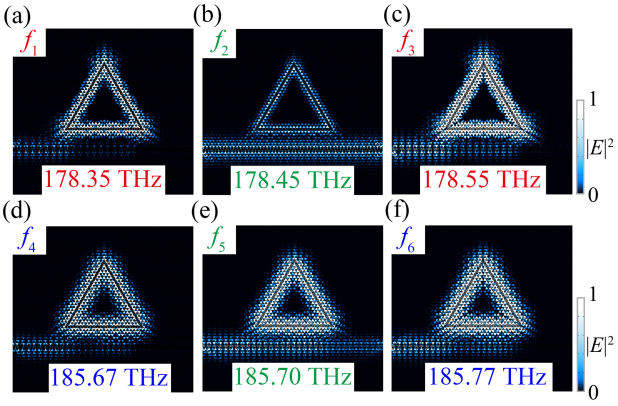

Fig. 5. Electric field distributions of a bandpass notch filter at various frequencies. (a)–(f) The electric field amplitude intensity distribution of the bandpass notch filter at frequencies 178.35, 178.45, 178.55, 185.67, 185.70, and 185.77 THz.

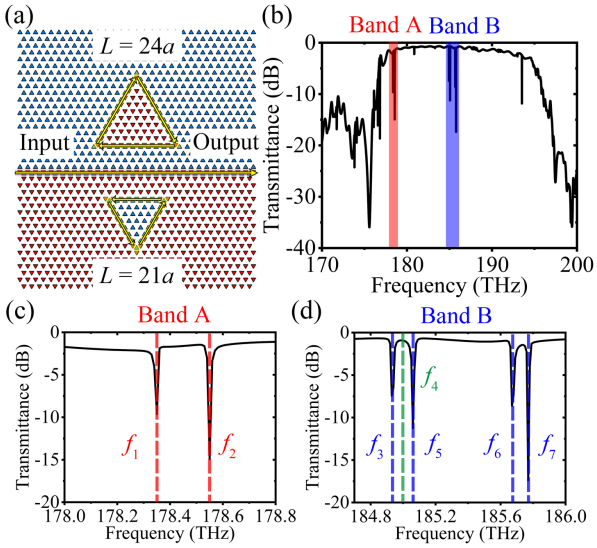

Fig. 6. Dual-cavity bandpass notch filter and transmission characteristics. (a) A schematic diagram of a dual-cavity bandpass notch filter composed of upper and lower dual-cavity and topological straight waveguide coupling. (b) Transmittance spectra of a dual-cavity band notch filter. (c) and (d) Transmittance spectra of the dual-cavity bandpass notch filter in Band A (178.0–178.8 THz) and Band B (184.8–186.0 THz).

short wavelength band. Based on the above ideas, we place triangular resonators with different side lengths above and below the topological straight waveguide, as shown in Fig. 6(a). When the triangular resonator with the side lengths $L = 24a$ and $L = 21a$ is combined with the topological straight waveguide, we find that the transmittance at the original resonant frequency is closer to zero than in the case of a single resonator because the resonance effect between the triangular resonators with different side lengths is partially overlapped, which makes the coupling of the system closer to the adjacent coupling condition [49], as shown in Fig. 6(b).

In addition, the transmission spectra of Bands A and B were plotted separately to analyze their properties, as shown in Figs. 6(c) and 6(d). Analysis of the spectrogram shows that a new

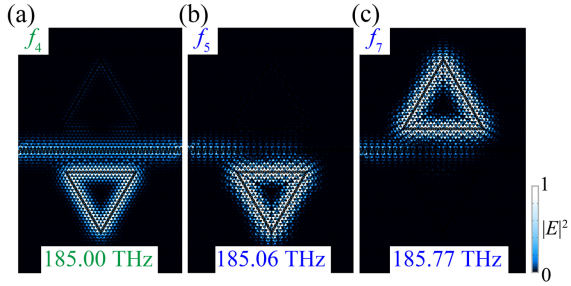

Fig. 7. Electric field distributions of a two-Cavity bandpass notch filter at different frequencies. (a)–(c) Electric field amplitude intensity distribution of the two-cavity bandpass notch filter at frequencies 185.00, 185.06, and 185.77 THz.

set of resonant frequencies (f_3 and f_5) emerges in the composite structure without changing the original resonant frequencies, while the frequencies in the bandgap still maintain high transmittance, as shown in Figs. 7(a)–7(c). As shown in Fig. 6, it is evident that the 3 dB bandwidths of resonant frequencies f_1, f_2, f_6, and f_7 remain unaffected. The newly observed resonant frequencies f_3 and f_5 exhibit 3 dB bandwidths of 0.03 and 0.02 THz, respectively, with corresponding suppression ratios of 7.43 and 11.23 dB. Compared with the filter with a single resonator structure, the filter with this combined structure not only has a significant improvement in the filtering effect, which can more effectively suppress the optical signal of a specific frequency (the suppression ratio of the resonant frequency f_7 is measured as 17.38 dB.) but also significantly increases the number of notches as a whole, which greatly enriches the frequency selection diversity of the filter. Therefore, the combination of resonators with different side lengths on topological straight waveguides can realize the flexible control of the number of resonant frequencies, positions, and filtering performance, and then significantly improve the filtering performance of the filter.

3. CONCLUSION

In summary, we designed a kind of bandpass notch filter based on a valley photonic crystal with topological properties. The filter is composed of a topological straight waveguide and a triangular resonator, and its design concept makes clever use of the principle of topological photonics, which is of great significance for effectively reducing the light scattering problem caused by large-angle turning in the integrated optical path. Based on a fully dielectric silicon material operating in the communication wavelength range, we designed a triangular resonator with topological properties, which achieves a high Q value (3.5226×10^8) at a resonant frequency of 185.77 THz due to the unique spin-valley locking effect of the valley photonic crystal. In order to further expand the performance and functionality of the filter, we construct different combinations of bandpass notch filter structures, including the combination of single cavity and topological straight waveguide, and the combination of double cavity and topological straight waveguide. The simulation results show that multiple resonant frequencies can appear in a relatively short band by reasonably combining triangular resonators with different side lengths, which effectively improves the filtering performance of the filter, so that it

can selectively filter the light waves of a specific frequency more accurately and greatly improves the frequency selectivity and resolution of the filter. Due to their unique advantages, bandpass notch filters based on topology protection can be widely used in more complex integrated optical devices. For example, cascaded high-order filters and low-crosstalk wavelength division multiplexing (WDM) devices have broad application prospects and great development potential in optical communication and on-chip integrated optical devices. They are expected to promote technological progress and industrial development in related fields.

However, we also recognized that there were some limitations and challenges to the design. First, the manufacturing complexity of triangular resonators presents practical challenges. The precise control of the size and position of the triangular air holes places high demands on microfabrication technology. Second, the coupling optimization between the triangular resonator and the topological straight waveguide requires fine tuning, and the coupling spacing can only be taken as an integer multiple of $\frac{\sqrt{3}}{2}a$ due to the geometry of the valley photonic crystal. Finally, the results presented in this article are based on simulations. In practice, factors such as material dispersion, propagation loss, and the effects of environmental conditions are more complex and can affect the actual performance of the equipment. These factors need to be further verified and studied experimentally to ensure the robustness and reliability of the filter in real-world scenarios.

Funding. National Natural Science Foundation of China (12174307).

Disclosures. The authors declare no conflicts of interest.

Data availability. No data were generated or analyzed in the presented research.

REFERENCES

1. H. Saghaei, M. Soroosh, M. J. Maleki, *et al.*, "High-performance and compact photonic crystal channel drop filter using p-shaped ring resonator," Results Opt. **21**, 100817 (2025).
2. Y. Awane, T. Inoue, and S. Noda, "Two-wavelength non-dispersive infrared sensing systems using stacked electrically controllable photonic-crystal band-pass filters," Opt. Express **32**, 31948–31955 (2024).
3. L. Gu, Q. Yuan, Q. Zhao, *et al.*, "A topological photonic ring-resonator for on-chip channel filters," J. Lightwave Technol. **39**, 5069–5073 (2021).
4. M. L. N. Chen, L. J. Jiang, Z. Lan, *et al.*, "Pseudospin-polarized topological line defects in dielectric photonic crystals," IEEE Trans. Antennas Propag. **68**, 609–613 (2020).
5. M. Youcef Mahmoud, G. Bassou, and F. Metehri, "Channel drop filter using photonic crystal ring resonators for CWDM communication systems," Optik **125**, 4718–4721 (2014).
6. Y. Gao, Y. He, J. Si, *et al.*, "Waveguide–cavity coupling system based on topological edge states and corner states in kagome photonic crystals," Adv. Quantum Technol. **7**, 2300265 (2023).
7. E. Archer, S. Hillebrandt, C. Keum, *et al.*, "Accurate efficiency measurements of organic light-emitting diodes via angle-resolved spectroscopy," Adv. Opt. Mater. **9**, 2000838 (2020).
8. K. S. Thakuri, T. Cleary, D. Allemeier, *et al.*, "Defect engineering in organic semiconductor based metal-dielectric photonic crystals," Sci. Rep. **14**, 29052 (2024).
9. T. Ochiai and J. Sánchez-Dehesa, "Localized defect modes in finite metallic two-dimensional photonic crystals," Phys. Rev. B **65**, 245111 (2002).
10. J. Xia, Q. Qiao, G. Zhou, *et al.*, "Opto-mechanical photonic crystal cavities for sensing application," Appl. Sci. **10**, 7080 (2020).
11. G. Bae, H. Park, and J. D. Lee, "Universal time delays in the inelastic core level photoemission of metals," Phys. Rev. B **103**, 165413 (2021).
12. A. Li, T. Van Vaerenbergh, P. De Heyn, *et al.*, "Backscattering in silicon microring resonators: a quantitative analysis," Laser Photonics Rev. **10**, 420–431 (2016).
13. S. Benchabane, L. Robert, J.-Y. Rauch, *et al.*, "Highly selective electroplated nickel mask for lithium niobate dry etching," J. Appl. Phys. **105** (2009).
14. R. Geiss, S. Diziain, M. Steinert, *et al.*, "Photonic crystals in lithium niobate by combining focussed ion beam writing and ion-beam enhanced etching," Phys. Status Solidi A **211**, 2421–2425 (2014).
15. R. Wu, J. Zhang, N. Yao, *et al.*, "Lithium niobate micro-disk resonators of quality factors above 107," Opt. Lett. **43**, 4116 (2018).
16. R. Gao, H. Zhang, F. Bo, *et al.*, "Broadband highly efficient nonlinear optical processes in on-chip integrated lithium niobate microdisk resonators of Q-factor above 108," New J. Phys. **23**, 123027 (2021).
17. R. Gao, N. Yao, J. Guan, *et al.*, "Lithium niobate microring with ultrahigh Q factor above 108," Chin. Opt. Lett. **20**, 011902 (2022).
18. J. Ma, X. Xi, and X. Sun, "Topological photonic integrated circuits based on valley kink states," Laser Photonics Rev. **13**, 1900087 (2019).
19. L. He, H. Y. Ji, Y. J. Wang, *et al.*, "Topologically protected beam splitters and logic gates based on two-dimensional silicon photonic crystal slabs," Opt. Express **28**, 34015 (2020).
20. H. Wang, L. Sun, Y. He, *et al.*, "Asymmetric topological valley edge states on silicon-on-insulator platform," Laser Photonics Rev. **16**, 2100631 (2022).
21. P. Zhang, J. Zhang, L. Gu, *et al.*, "Compact on-chip power splitter based on topological photonic crystal," Opt. Mater. Express **14**, 1390–1397 (2024).
22. G.-J. Tang, X.-D. Chen, L. Sun, *et al.*, "Broadband and fabrication-tolerant 3-db couplers with topological valley edge modes," Light Sci. Appl. **13**, 166 (2024).
23. M. Jalali Mehrabad, A. P. Foster, N. J. Martin, *et al.*, "Chiral topological add–drop filter for integrated quantum photonic circuits," Optica **10**, 415 (2023).
24. A. Kumar, M. Gupta, P. Pitchappa, *et al.*, "Phototunable chip-scale topological photonics: 160 Gbps waveguide and demultiplexer for Thz 6G communication," Nat. Commun. **13**, 5404 (2022).
25. L. Sun, H. Wang, Y. Zhang, *et al.*, "Silicon topological photonic bandpass/notch filter," in *Conference on Lasers and Electro-Optics, CLEO_SI* (Optica Publishing Group, 2020), paper STu3J.6.
26. G.-J. Tang, X.-D. Chen, F.-L. Shi, *et al.*, "Frequency range dependent topological phases and photonic detouring in valley photonic crystals," Phys. Rev. B **102**, 174202 (2020).
27. C. Lu, C. Wang, M. Xiao, *et al.*, "Topological rainbow concentrator based on synthetic dimension," Phys. Rev. Lett. **126**, 113902 (2021).
28. C. Lu, Y.-Z. Sun, C. Wang, *et al.*, "On-chip nanophotonic topological rainbow," Nat. Commun. **13**, 2586 (2022).
29. H. Zhang, L. Qian, C. Wang, *et al.*, "Topological rainbow based on graded topological photonic crystals," Opt. Lett. **46**, 1237 (2021).
30. M. X. Li, Y. K. Wang, M. J. Lu, *et al.*, "Dual-mode of topological rainbow in gradual photonic heterostructures," J. Phys. D Appl. Phys. **55**, 095103 (2021).
31. Y.-C. Lin, S.-H. Chou, and W.-J. Hsueh, "Robust high-Q filter with complete transmission by conjugated topological photonic crystals," Sci. Rep. **10**, 7040 (2020).
32. C.-C. Lu, H.-Y. Yuan, H.-Y. Zhang, *et al.*, "On-chip topological nanophotonic devices," Chip **1**, 100025 (2022).
33. S. Barik, A. Karasahin, S. Mittal, *et al.*, "Chiral quantum optics using a topological resonator," Phys. Rev. B **101**, 205303 (2020).
34. L. Sun, X. Li, P. Hu, *et al.*, "Thermally tunable add-drop filter based on valley photonic crystals for optical communications," Nanophotonics **13**, 4459–4470 (2024).
35. R. Kumar, K. M. Rohith, S. Pandey, *et al.*, "Terahertz tunable bandstop filter using topological valley photonic crystals," Appl. Opt. **63**, 104–111 (2023).

36. Y. Gong, S. Wong, A. J. Bennett, *et al.*, "Topological insulator laser using valley-hall photonic crystals," ACS Photonics **7**, 2089–2097 (2020).
37. K. Y. Fong, W. H. P. Pernice, M. Li, *et al.*, "High Q optomechanical resonators in silicon nitride nanophotonic circuits," Appl. Phys. Lett. **97** (2010).
38. B. Bahari, A. Ndao, F. Vallini, *et al.*, "Nonreciprocal lasing in topological cavities of arbitrary geometries," Science **358**, 636–640 (2017).
39. J. Hong and M. J. Lancaster, *Microstrip Filters for RF/Microwave Applications* (Wiley, 2001).
40. J. Lu, C. Qiu, L. Ye, *et al.*, "Observation of topological valley transport of sound in sonic crystals," Nat. Phys. **13**, 369–374 (2016).
41. G.-C. Wei, Z.-Z. Liu, D.-S. Zhang, *et al.*, "Frequency dependent wave routing based on dual-band valley-hall topological photonic crystal," New J. Phys. **23**, 023029 (2021).
42. Q. Chen, L. Zhang, M. He, *et al.*, "Valley-hall photonic topological insulators with dual-band kink states," Adv. Opt. Mater. **7**, 1900036 (2019).
43. X.-T. He, E.-T. Liang, J.-J. Yuan, *et al.*, "A silicon-on-insulator slab for topological valley transport," Nat. Commun. **10**, 872 (2019).
44. D. Yang, C. Wang, W. Yuan, *et al.*, "Silicon on-chip side-coupled high-Q micro-cavities for the multiplexing of high sensitivity photonic crystal integrated sensors array," Opt. Commun. **374**, 1–7 (2016).
45. M. Minkov, V. Savona, and D. Gerace, "Photonic crystal slab cavity simultaneously optimized for ultra-high Q/V and vertical radiation coupling," Appl. Phys. Lett. **111** (2017).
46. L. Liu, C. Ma, M. Ye, *et al.*, "Photonic crystal nanobeam cavity with a high experimental Q factor exceeding two million based on machine learning," J. Lightwave Technol. **40**, 7150–7158 (2022).
47. E. Waks and J. Vuckovic, "Coupled mode theory for photonic crystal cavity-waveguide interaction," Opt. Express **13**, 5064 (2005).
48. S. Olivier, H. Benisty, C. Weisbuch, *et al.*, "Coupled-mode theory and propagation losses in photonic crystal waveguides," Opt. Express **11**, 1490 (2003).
49. M. Cai, O. Painter, and K. J. Vahala, "Observation of critical coupling in a fiber taper to a silica-microsphere whispering-gallery mode system," Phys. Rev. Lett. **85**, 74–77 (2000).